Journal of Inorganic and Organometallic Polymers and Materials (2020) 30:2952–2970
https://doi.org/10.1007/s10904-019-01435-2

Electronic Structure, Morphological Aspects, and Photocatalytic Discoloration of Three Organic Dyes with $MgWO_4$ Powders Synthesized by the Complex Polymerization Method

A. F. Gouveia[1] · V. E. M. Vieira[1] · J. C. Sczancoski[2] · P. S. Lemos[2] · S. K. Rout[3] · N. S. Arul[4] · E. Longo[2] · L. S. Cavalcante[1]

Received: 26 November 2019 / Accepted: 30 December 2019 / Published online: 16 January 2020

Abstract

Heterogeneous photocatalytic (PC) degradation of organic dyes in aqueous solution with semiconductor oxides has been very effective in relation to conventional methods for the wastewater treatment. In this paper, $MgWO_4$ powder was synthesized by the complex polymerization method and heat-treated at 900 °C for 2 h. Their structure, morphology and optical behavior were characterized by different techniques. First-principles quantum mechanical calculations based on the DFT in the B3LYP level was employed to obtain their electronic band structure (EBS) and density of state (DOS). Moreover, we have investigated the PC properties for the discoloration of three organic dyes. XRD patterns indicate that $MgWO_4$ powders present a monoclinic structure. FE-SEM and TEM images showed that these powders are composed of several nanoparticles. UV–Vis spectrum displays an optical band gap of 4.33 eV, while EBS calculation showed a direct band gap value of 4.49 eV. DOS data revealed that the main orbitals involved in the electronic structure are O-2*p* orbitals in the valence band and W-5*d* orbitals in the conduction band. Finally, it was obtained the best PC activity of $MgWO_4$ powders with discoloration of 84% for bromocresol green dye, while the discoloration for methyl orange and rhodamine B dyes were 56% and 29%, respectively.

Electronic supplementary material The online version of this article (https://doi.org/10.1007/s10904-019-01435-2) contains supplementary material, which is available to authorized users.

✉ L. S. Cavalcante
laeciosc@bol.com.br

[1] PPGQ-GERATEC, Universidade Estadual do Piauí, Rua: João Cabral, N. 2231, P.O. Box 381, Teresina, PI 64002-150, Brazil

[2] CDMF-UFSCar, Universidade Federal de São Carlos, Departamento de Química e Engenharia de Materiais, P.O. Box 676, São Carlos, SP 13565-905, Brazil

[3] Department of Physics, Birla Institute of Technology, Mesra, Ranchi, India

[4] Department of Chemical and Biochemical Engineering, Dongguk University-Seoul, Seoul 04620, South Korea

Graphic Abstract

The electronic structure, morphology and photocatalytic properties of $MgWO_4$ powders synthesized by complex polymerization method calcinated at 900 °C for 2 h have been explained for the first time.

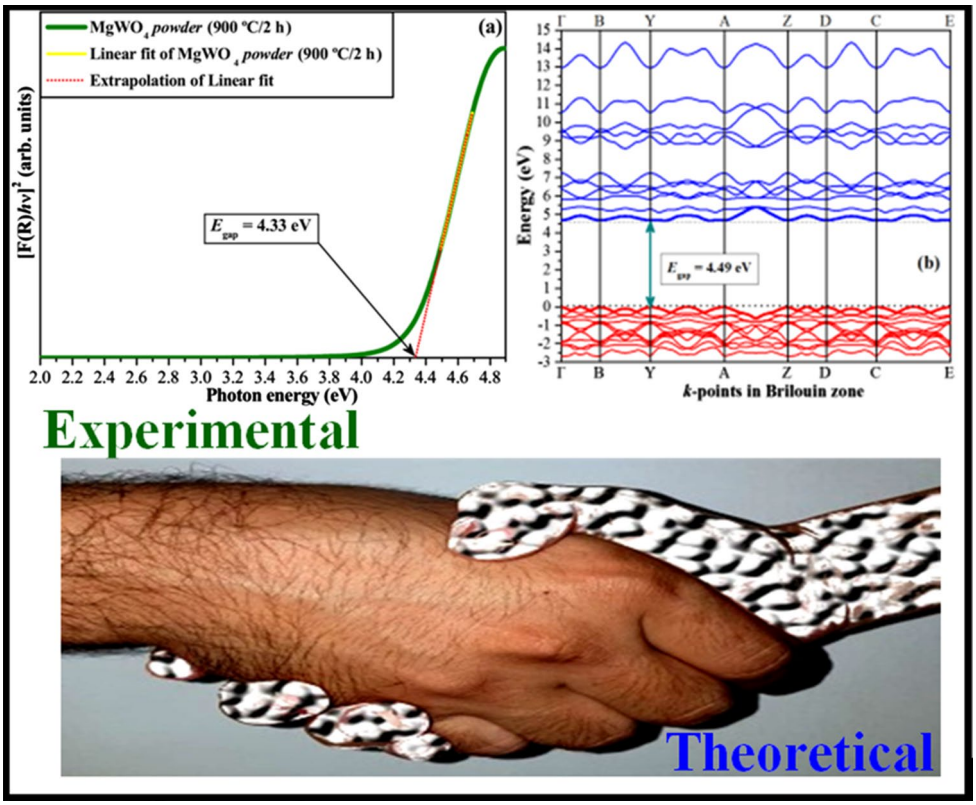

Keywords $MgWO_4$ powders · Rietveld refinement · Electronic band structure · Density of states · Photocatalysis

1 Introduction

In recent years, problems related to environmental issues have been one of the main concerns in the world [1, 2]. Water is a vital natural resource for all life-forms on Earth. Hence, there is an enormous interest of the modern society in the development of biological, physicochemical treatment techniques able to drastically reduce or remove the presence of harmful substances found in contaminated rivers, lakes, and groundwater. Particularly, organic dyes and pigments employed in leather or textile industries are considered environmental enemies when irresponsibly discharged in freshwater supplies [3, 4]. Generally, these types of contaminants are potentially toxic, carcinogenic and non-biodegradable, causing serious environmental damages to the fauna and aquatic botany of our planet [5]. As an alternative route in order to minimize these problems, the heterogeneous photocatalysis (HPC) has presented a high potential for the treatment of polluted water. HPC is a physical–chemical process based on the acceleration of photoreaction in the presence of a semiconductor catalyst [6]. This process has been scientifically explained by means of the reduction and oxidation of chemical species found in organic dyes by means of electron–hole pairs, generated between the valence band and the conduction band of the catalyst, during the absorption phenomenon of ultraviolet light/visible or sunlight. Different papers reported in the literature [7, 8] have explained in details these photocatalytic effects and others as adsorption properties with different types of inorganic materials.

In this way, the magnesium tungstate ($MgWO_4$) and other metal tungstates have been good canditates as photocatalytic semiconductors. Their general formula is AWO_4, where A is a divalent (A^{2+} = Mn, Ni, Fe, Co, and Zn; d-transition metals) designated as network modifier [9, 10]. The electronic structure of AWO_4 is designed to wolframite-type monoclinic structure with space group (P_2/c), symmetry point group (C_{2h}^4) and two molecular formula units per unit cell (Z = 2) [11]. All these tungstates have the same chemical coordination for the network former (W^{6+}) and network modifiers (A^{2+}), which are composed of distorted octahedral [WO_6] and [AO_6] clusters [12].

While analyzing the thermodynamic properties of $MgWO_4$, Guo and Kleppa [13] found that the enthalpy of formation (ΔH_f) at 298 K is − 73.9 K ± 4.8 kJ/mol. Moreover, Kazenas et al. [14] used high-temperature mass spectrometry and determined that the vapor pressure of $MgWO_{4(g)}$ (in atm) is − 28.737 ± 7.95/T, its enthalpy of sublimation is 652 K ± 20 kJ/mol, and its enthalpy of formation is − 867 ± 20 kJ/mol. In general, the preparation of this pure phase with monoclinic structure at room temperature is not possible due to its high crystallization temperature of approximately 900 °C [15]. Under hydrothermal conditions, it is only possible to obtain pure $MgWO_4$ crystals with tetragonal structure at 230 °C after 48 h [16]. It is not possible to prepare amorphous $MgWO_4$ at ambient temperature or with adjust of pH in alkaline solution. To prepare amorphous $MgWO_4$ or $MgWO_4{\cdot}H_2O$ the optimization of different parameters is required: heating the solution, stirring for a given number of days, pH control, or the use of a solvent or sonication to break the solvation energy that water molecules exert between the Mg^{2+} and WO_4^{2-} ions preventing them from self-attracting at pH ranging from 4 to 7 [17–19].

While difficulties can be encountered when synthesizing pure $MgWO_4$ powders, different synthesis methods have been reported in the literature for obtaining $MgWO_4$ ceramics, crystals, or powders with monoclinic structure via solid state reaction or mixed oxide route [20–22], mechanochemically assisted solid state [23], top-seeded solution growth [24], solid-state metathetic (SSM) route assisted by microwave irradiation [25], as well as co-precipitation/calcination [26] and hydrothermal/calcination [27]. Previous studies discuss the very good physicochemical properties and applicability of $MgWO_4$ ceramics, crystals or powders, mainly related to their luminescent [28–33] and microwave dielectric properties [34, 35]. However, the photocatalytic (PC) properties of $MgWO_4$ powder for the discoloration of following organic dyes: Rhodamine B (RhB), methyl orange (MO), and bromocresol green (BCG) have not been reported yet. Figures 1a–c show the molecular structures of RhB, MO, and BCG dyes, respectively.

Figure 1a displays the RhB cationic dye ($C_{28}H_{31}ClN_2O_3$) which exhibits a heterocyclic structure with four aromatic rings and a branched carbon chain. Figure 1b, c show that MO ($C_{14}H_{14}N_3NaO_3S$) and BCG ($C_{21}H_{14}Br_4O_5S$) are homocyclic anionic dyes with a branched carbon chain each, with two and three aromatic rings, respectively.

There is a great worldwide environmental concern regarding textile organic dyes and industrial contaminants being freely disposed in groundwater, rivers, and lake tributaries by the paper, textile and tanning industries [36, 37]. Industrial organic dyes are large fluvial water contaminants that cause serious environmental problems because they are potentially carcinogenic, toxic, non-biodegradable, and fish mortality [38, 39].

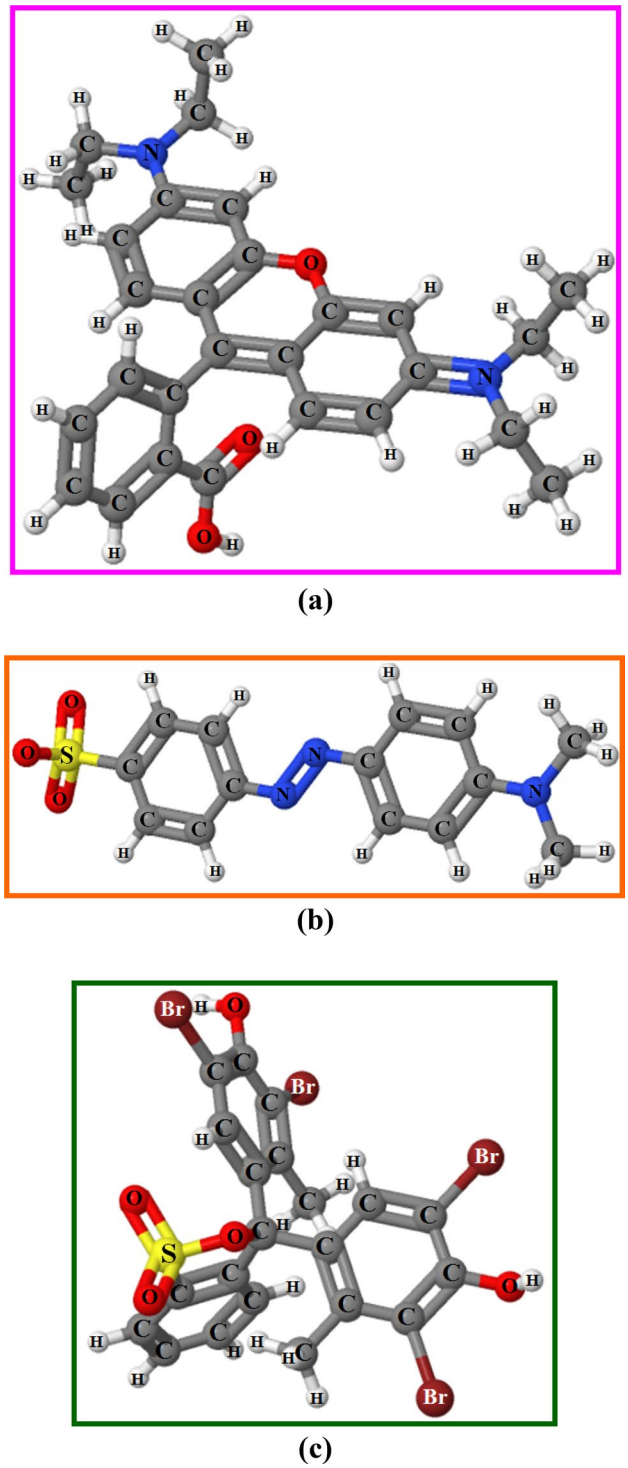

Fig. 1 Molecular structures of: **a** Rhodamine B, **b** Methyl Orange, and **c** Bromocresol Green

Globally, the production of organic dyes by the textile or printing industries is estimated at approximately 10,000 ton annually, 10% of which are discharged as industrial effluents without any prior treatment [40]. Rhodamine B, also known

as Basic Violet 10 is a well-known industrial dye commonly employed for dyeing cotton, clothes and also for preparing stamp pad ink and ballpoint pens [41]. This organic dye is non-volatile and highly soluble in water, methanol, and ethanol [42]. On the other hand, RhB is dangerous if swallowed by humans or animals, and can cause irritation to the skin, eyes and respiratory system [43]. Methyl orange, another organic dye, is used as a pH indicator due to its distinct red color in acidic media and yellow color in basic media [44, 45]. This azo organic dye has an Ar–N=N–Ar′ basic structure where Ar and Ar′ are aromatic rings and the unit containing the –N=N– bond, called the azo group, is a strong chromophore group which gives these compounds their bright colors. Many combinations of Ar–NH_2 and Ar′–NH_2 or Ar–OH are involved in the formation of azo bonds [46]. Moreover, as indicated by the literature [47, 48] MO dyes are very difficult to be mineralized or decomposed by oxides catalysts using ultraviolet (UV) or visible (Vis) light. Furthermore, BCG is a triphenylmethane type organic dye used as a pH indicator that can also be a highly toxic compound when inhaled or coming in contact with the skin and eyes [49, 50]. The decomposition of BCG by ZnO catalysts nanoparticles requires high irradiation time even under UV-light [51].

From a practical viewpoint, semiconductor photocatalysis is an alternative method for the removal of soluble toxic compounds, particularly because of its significant advantages: it has low cost, it is easy to handle, the reaction is promoted using energy of Vis- or UV-light source, and there is minimal secondary waste generated [52].

Therefore, in this paper, we report a detailed theoretical and experimental study for $MgWO_4$ powder synthesized by complex polymerization method at 90 °C for 4 h. We also report for the first time the thermal pre-treatment of the resin type precursor at 350 °C for 10 h followed by calcination at 900 °C for 2 h. The obtained $MgWO_4$ powder was characterized using X-ray diffraction (XRD) patterns and Rietveld refinement analysis. The morphological features and chemical composition were examined by field emission-scanning electron microscope (FE-SEM), transmission electron microscopy (TEM), high-resolution transmission electron microscopy (HR-TEM) and energy dispersive X-ray spectrometry (EDS). The optical band gap of the obtained $MgWO_4$ powder were examined using UV–Vis spectroscopy. The electronic band structure, density of states (DOS), and electron density maps of $MgWO_4$ crystals were theoretically calculated to understand the phenomenon of structural properties. Finally, we investigated the PC properties of $MgWO_4$ powder under UV light through the presence of the effects and distortions in the octahedra present in the ordered monoclinic lattice, establishing its usefulness in the discoloration of the three organic dyes: RhB, MO, and BCG.

2 Materials and Methods

2.1 Experimental Details

The $MgWO_4$ powder was synthesized by using the modified complex polymerization (CP) method [53]. Magnesium nitrate hexahydrate [$Mg(NO_3)_2{\cdot}6H_2O$, 99% purity, Vetec®], tungstic acid (H_2WO_4, 99% purity, Aldrich®), ethylene glycol ($C_2H_6O_2$, 99.5% purity, Contemporary Chemistry Dynamics LTDA®) and citric acid ($C_6H_8O_7$, 99.5% purity, Sigma-Aldrich®) were used as raw materials. The following steps were followed: (I) First we dissolved citric acid in deionized water at room temperature for 10 min. (II) Subsequently, we dissolved H_2WO_4 into the aqueous citric acid solution at 85 °C for 5 h under constant stirring to allow the homogenization and formation of the tungsten citrate solution, while also using 10 mL of ammonium hydroxide solution ($NH_3{\cdot}H_2O$ 30% purity, Contemporary Chemistry Dynamics LTDA®). (III) After the homogenization of the tungsten citrate solution, the gravimetric procedure using 4 crucibles was performed in order to find the precise molar concentration of the tungsten citrate (grams of tungsten citrate/mol of WO_3). (IV) After optimization, the appropriate molar concentration of $Mg(NO_3)_2{\cdot}6H_2O$ was added to the tungsten citrate. The citrate solution containing both cations was again stirred for 4 h at 90 °C to produce a homogeneous solution and then the solution pH was adjusted to 7 by adding $NH_3{\cdot}H_2O$. This procedure is employed to avoid the chemical precipitation of magnesium citrate ($C_6H_6MgO_7$), which is favored in acidic solutions [54]. (V) After stabilizing the pH, we added $C_6H_8O_7$ to promote the polyesterification reaction [55]. The citric acid and metal molar ratio was fixed as 3:1 and the citric acid to ethylene glycol mass ratio was taken as 60:40 to advance the citrate polymerization [56]. (VI) The polymerized solution was slowly heated to allow the evaporation of water and formation of the polymeric resin. (VII) The obtained polymeric resin was then placed in a conventional furnace and heated to 350 °C for 10 h using a 1 °C/min heating rate. The precursor powder was heat treated at 900 °C for 2 h at a 1 °C/min heating rate in air.

2.2 Characterizations

$MgWO_4$ powder heat treated at 900 °C for 2 h was structurally characterized using XRD with a LabX XRD-6000 diffractometer (Shimadzu, Japan) with Cu Kα radiation ($\lambda = 0.15406$ nm) with a scan rate of 2°/min. The Rietveld analysis was conducted from 10° to 110° 2θ range with a step rate of 0.02° and scan rate of 1°/min. This structural refinement method has several advantages over conventional quantitative analysis methodologies: whole

pattern-fitting algorithms are used, so all lines for each phase are explicitly considered; furthermore, even significantly overlapping lines are usually not a problem [57]. The structural refinement was performed using the ReX software version 0.9.1 [58], which revealed the Rietveld texture and stress analysis [59]. The structural refinement quality is generally checked using the R values (R_p, R_{exp}, R_{wp}) and GoF. The difference between the observed and calculated patterns is the best way to judge the success of the Rietveld refinement. The optimized parameters were the scalar factor, 2θ offsets, sample position, background with polynomial coefficients, adjusting the diffraction peaks shape with Pseudo-Voigt function, basic phase, crystal structure, cell parameters (a, b, c), angles (α, β, γ), lattice strain, and isotropic U factor [60]. The morphology investigations of $MgWO_4$ powders microcrystals were observed in a field emission-scanning electron microscope (FE-SEM) of Quanta™ 250-FEG model (FEI® Company, Netherlands) operated with acceleration voltage from 15 to 20 kV. Transmission electron microcopy (TEM), high-resolution transmission electron microscopy (HRTEM) images and chemical analysis using energy dispersive X-ray spectroscopy (EDS) were obtained with a FEI Tecnai G2 F20 microscope operating at 200 kV. The samples were prepared by drop a diluted suspension over a 400-mesh carbon coated copper grid under semi permeable paper to dry the excess of solution. UV–Vis spectra were performed using a Shimadzu Scientific Instruments spectrometer (Model UV-2600, Japan) operated in diffuse reflectance mode. The specific surface area of the microcrystals was recorded with an ASAP 2000 Phys/Chemisorption unit (Micromeritics, USA) and estimated by the Brunauer–Emmett and Teller (BET) methodology [61].

2.3 Photocatalytic Activity Measurements

The PC properties of $MgWO_4$ powder were tested in aqueous solution under UV-light towards the discoloration of three dyes: [9-(2-carboxyphenyl)-6-diethylamino-3-xanthenylidene]-diethylammonium chloride, also known as tetraethylated Rhodamine or Rhodamine B (RhB; 95%, Sigma-Aldrich, with a $\lambda_{max} = 543$ nm), sodium 4-{[4-(dimethylamino)phenyl]diazenyl}benzene-1-sulfonate, known as methyl orange (MO, 85%, Sigma-Aldrich, with a $\lambda_{max} = 505$ nm), and 2,6-dibromo-4-[7-(3,5-dibromo-4-hydroxy-2-methyl-phenyl)-9,9-dioxo-8-oxa-9λ6-thiabicyclo[4.3.0]nona-1,3,5-trien-7-yl]-3-methyl-phenol, or Bromocresol green (BCG, 95%, Sigma-Aldrich, with a $\lambda_{max} = 616$ nm). All solutions were prepared in deionized water. The catalyst (30 mg) was added to 250 mL beakers, along with 50 mL of 1×10^{-5} mol/L RhB, MO, and BCG solutions, respectively. The pH values of dyes solutions were 6.25, 4.55, and 4.75, respectively. These pH were measured in a Benchtop pH Meter (QUIMIS®) model Q400AS. The suspensions were ultrasonicated for 2 min in an ultrasonic cleaner (Model CPX1800H, Branson®) with a 42 kHz frequency before being illuminated and then stored in the dark for 5 min to allow the saturated absorption of RhB, MO and BCG dyes onto the catalyst. The beakers were then placed in a photoreactor at 25 °C and illuminated by four UV-C lamps (Moran Ligth®) with power of 18 W each, the luminosity of 145 lumens, beam angle at 320° and maximum intensity at 254 nm the source with the distance about 45 cm of the surface dye solution. At 10 min intervals, 3 mL aliquots were removed and centrifuged at 8500 rpm for 10 min to remove the crystals from the suspension. The variations in the absorption band maximum of the catalysts were monitored by UV–Vis spectroscopy.

2.4 Computational Method

The theoretical calculations to study the optical properties of $MgWO_4$ structure were performed using the CRYSTAL14 software package [62]. The computational methodology is based on the DFT associated with the hybrid functional B3PYP composed of Becke's three-parameter hybrid non-local exchange functional [63] combined with a Lee–Yang–Parr gradient-corrected correlation functional [64]. In order to describe the atomic centers of $MgWO_4$ crystal, we used the 8-511d1G and 6-31d1 bases sets for Mg and O atoms, respectively, which were obtained from the Crystal website [65]. The large-core effective core potential was derived by Hay and Wadt, and modified by Cora et al. [66] for W atoms. The electronic band structure (EBS) and the DOS of the $MgWO_4$ structure were calculated using the Properties 14 function of the CRYSTAL14 software and constructed along the appropriate high-symmetry directions of the corresponding irreducible Brillouin zone [67].

3 Results and Discussion

3.1 XRD Patterns and Rietveld Refinement Analysis

Figures 2a, b show the XRD patterns and Rietveld refinement plot for the $MgWO_4$ powder synthesized using the CP method and calcined at 900 °C for 2 h, respectively.

The degree of structural periodicity of a crystalline lattice in tungstate-type's oxide materials can be investigated using XRD [68]. The $MgWO_4$ powder heat-treated at 900 °C for 2 h shown in Fig. 2a exhibited monoclinic structure of $MgWO_4$ which is in consistence with the respective Inorganic Crystal Structure Database (ICSD) card No. 22357 [69]. The amorphous materials and structural evolution of

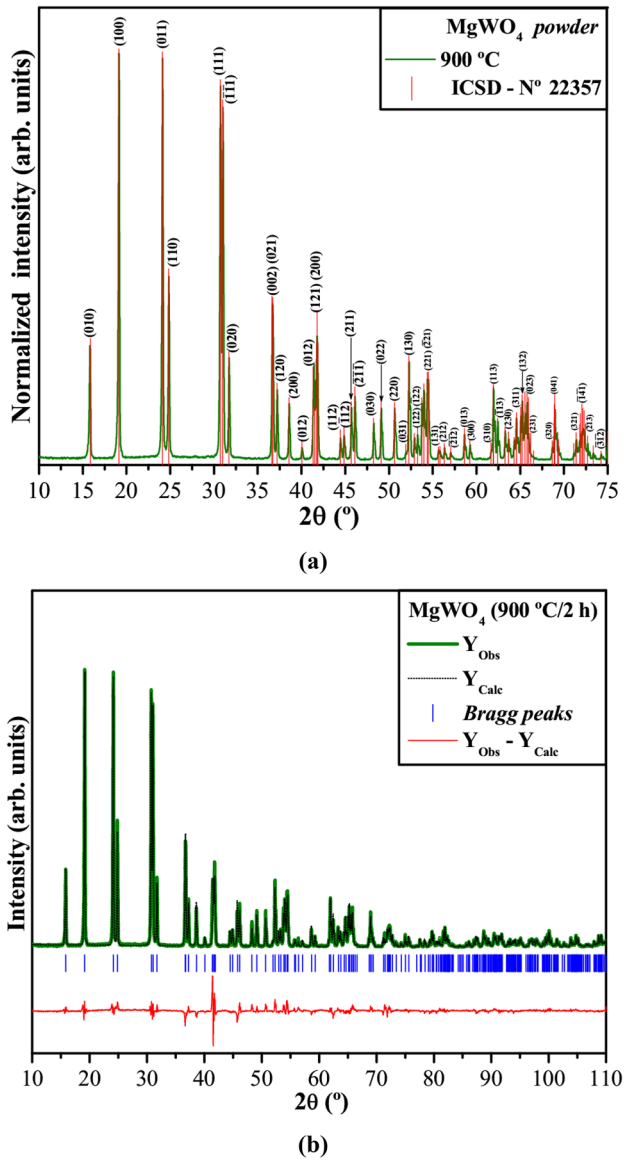

Fig. 2 **a** XRD patterns and **b** Rietveld refinement plot of $MgWO_4$ powder heat treated at 900 °C for 2 h. The vertical lines in red indicate the position and relative intensity of XRD patterns for the $MgWO_4$ phase reported in ICSD cif file No. 22357

α-,β-$MgWO_4$ phases are shown in the (Supporting Information (SI) section as shown in Figs. SI1. In addition, we have performed a structural refinement using the Rietveld method to confirm the presence of $MgWO_4$ sample heat-treated at 900 °C for 2 h [70]. As can be observed in Fig. 2b, our $MgWO_4$ powder has a wolframite-type monoclinic structure with space group (P_2/c), symmetry point group (C_{2h}^4), and two molecular formula units per unit cell (Z = 2). In general, slight differences in the intensity scale were identified between the experimental and calculated XRD patterns, as described by the $Y_{Obs} - Y_{Calc}$ line which indicates the reliability of the results. More details on the obtained data are displayed in Table 1 below.

From Table 1, the fit parameters (R_p, R_{wp}, R_{exp}, and GoF) suggest that the refinement results are very reliable. In general, small variations in the atomic positions of O atoms were identified, while Mg and W atoms are fixed in their respective positions within the structure. Likewise, the lattice parameters and atomic positions obtained from the Rietveld refinement analysis were used to start the optimization of theoretical model, which are listed in Table 2.

From the Rietveld refinement data for the $MgWO_4$ crystal (Table 1), the DFT theoretical calculations were performed in order to optimize all the parameters required to obtain the ideal structure in a vacuum. The optimized parameters are listed in Table 2. Comparing the experimental and theoretical results, it is possible to verify a little variation in the lattice parameters as in the atomic coordination, resulting in a slightly compressed theoretical structure.

3.2 Clusters Coordination's and Electron Density Models Analysis

Figure 3 shows a schematic representation of the monoclinic structure of $MgWO_4$ crystal.

The monoclinic structure of the $MgWO_4$ crystal was modeled on a visualization system for electronic and structural analysis (VESTA) software [71, 72], by using the lattice parameters and atomic positions obtained from Rietveld refinement data listed in Table 1. It is observed from Fig. 3

Table 1 Lattice parameters, unit cell volume, atomic coordinates, and site occupation obtained from Rietveld refinement data for $MgWO_4$ powder

Atoms	Wyckoff	Site	*x*	*y*	*z*	U_{iso} [Å^2]
Mg	2*f*	2	0.5	0.673145	0.25	0.011545
W	2*e*	2	0	0.182864	0.25	0.005157
O1	4*g*	1	0.209938	0.114030	0.919725	0.065592
O2	4*g*	1	0.261428	0.356497	0.393390	0.091767

$a = 4.69045(3)$ Å; $b = 5.67767(7)$ Å; $c = 4.931(1)$ Å; $\alpha = \gamma = 90°$; $\beta = 89.2942°$; and V = 131.307(1) Å^3; $R_p = 10.84\%$; $R_{exp} = 5.72\%$; $R_{wp} = 15.27\%$ and GoF = 2.67

Table 2 Lattice parameters, unit cell volume, atomic coordinates and site occupation obtained by DFT calculations for the optimized $MgWO_4$ crystal

Atoms	Wyckoff	Site	*x*	*y*	*z*
Mg	2*f*	2	0.5	0.68854	0.25
W	2*e*	2	0.0	0.21050	0.25
O1	4*g*	1	0.22161	0.10845	0.96001
O2	4*g*	1	0.24760	0.38658	0.41119

$a = 4.6723$ Å; $b = 5.7731$ Å; $c = 4.8519$ Å; $\alpha = \gamma = 90°$; $\beta = 89.0652°$; and $V = 130.8556$ Å^3

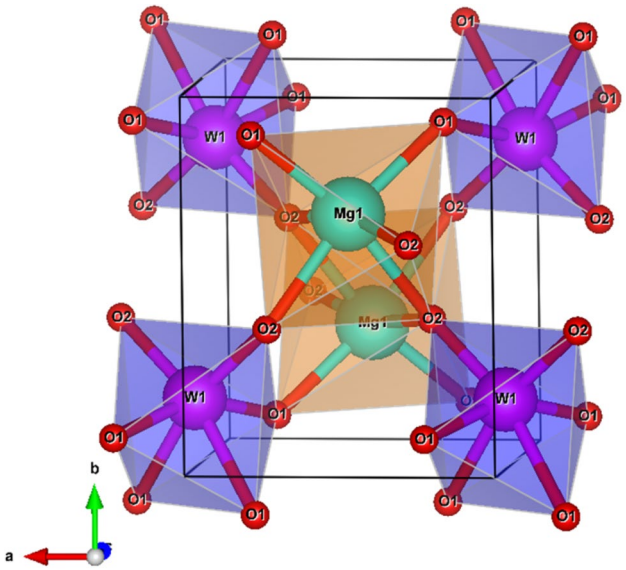

Fig. 3 Unit cell representations for $MgWO_4$ crystals with monoclinic structure

that the distorted octahedral [MgO_6] and [WO_6] clusters are octahedron-type polyhedrons with 6 vertices, 8 faces and 12 edges [73]. In principle, these $MgWO_4$ powder presents some variations in both O–Mg–O and O–W–O bond angles and lengths. This behavior results in distortions in octahedral [MgO_6] and [WO_6] clusters with distinct degrees of order–disorder in the lattice.

Figures 4a–c show electron density models in the (111), (010), and (121) planes for $MgWO_4$ crystals, respectively.

The electron density models were calculated by using the Fourier transform for structure factors from the structure parameters and atomic scattering factors of free atoms obtained from the Rietveld refinement for $MgWO_4$ powder obtained by the CP method, where the amorphous powder precursor was heat treated at 900 °C for 2 h. The data were used in VESTA software version 3.4.5 [71, 72] to model the electron density map. These figures display color scales for each plane, which indicates zones with high and low electronic densities. In Fig. 4a, the blue regions are related to the absence of electronic charge, while the red areas exhibit a high electronic density in the (111) plane. Moreover, it is possible to verify the presence of distributions non-homogeneous near the O–Mg–O bonds related to an atomic displacement, suggesting the existence of large distortions between Mg and O atoms (Fig. 4a). We found two W atoms and three O atoms in the (010) plane due to the presence of distortions in octahedral [WO_6] clusters (Fig. 4b). Finally, (121) plane reveals the Mg and W atoms able to share the same O atom. This behavior is displayed by the differences at the bond distance between O–Mg–O and O–W–O (Fig. 4c).

3.3 FE-SEM, TEM and HT-TEM Analyses

FE-SEM images were employed to monitor the morphological aspects of $MgWO_4$ powder synthesized using the CP method and heat treated at 900 °C for 2 h. Figure 5a–d shows the FE-SEM images at low and high magnifications of $MgWO_4$ powders.

Figure 5a reveals that the $MgWO_4$ powders are composed of several particles with irregular morphology and non-uniform agglomerated particles. The heat treatment performed at low temperature initially induces a decomposition process of residual organic compounds arising from citric acid and ethylene glycol. The formation of the pores at particles is promoted by means of this decomposition slow, which reduced by the particles growth, forming large aggregated regions with irregular shapes. The dotted yellow square in Fig. 5a and at high magnification in Fig. 5b, suggest that the thermal energy favors the diffusion mechanism, leading to the microparticles into a more dense mass. Figure 5c displays the SEM images of $MgWO_4$ powder heat-treated at 900 °C for 2 h resulted in the necking between the grains, as shown in Fig. 5d by means of individual $MgWO_4$ particles which is composed by several nanoparticles. Morever, the Fig. 5e–g display the TEM, HR-TEM images and SAED patterns of $MgWO_4$ nanopowders heat-treated at 900 °C for 2 h under air atmosphere. A close examination of low magnification TEM micrographs in Fig. 5a revealed that the powders are formed by the agglomeration of several small particles with irregular morphologies and different particle sizes. These morphological feactures can be arising from a non-controlled particle growth. Figure 5e shows a high magnification TEM micrograph of several nanoparticles, where the crystallographic planes were verified by HR-TEM. The HR-TEM micrograph taken from the selected area marked by the spherical-like indicated that the planes present an interplanar spacing of 0.2846 nm, which was identified as belonging to the (020) plane, as displays in Fig. 5f. In this context, the respective SAED pattern (Fig. 5g) confirmed that these particles are well-crystallized, presenting a single

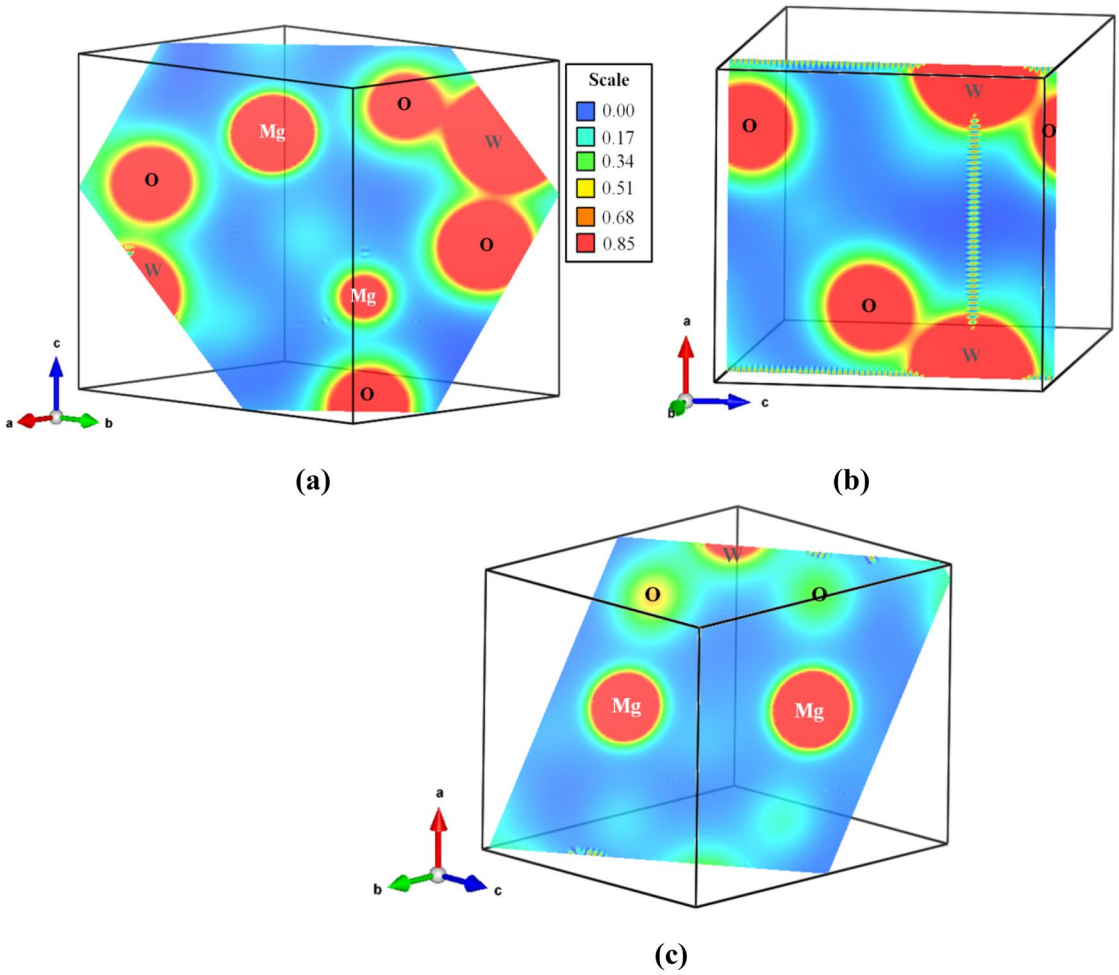

Fig. 4 Electron density maps in the **a** (111), **b** (010), and **c** (121) planes of $MgWO_4$ crystals

phase with wolframite-type monoclinic structure. Finally, Fig. 5h shows an EDS spectrum analysis for this $MgWO_4$ nanopowders. This EDS spectrum revealed that the powders are chemically composed of magnesium (Mg), tungsten (W) and oxygen (O). Therefore, this result confirms that the heat treatment performed at 900 °C for 2 h under air atmosphere is able to allow the formation of pure $MgWO_4$ nanopowders. The presence of Cu atoms in the spectrum is because of the carbon-coated copper grids. The quantitative results on the chemical composition analysis presented the following results of 69.8% for W, 26.9% for O 3.3% for Mg, respectively.

3.4 Ultraviolet–Visible Spectroscopy and Electronic Band Structures Analysis

The optical band gap energy (E_{gap}) was calculated using the Kubelka–Munk, which are based on the transformation of diffuse reflectance measurements and can estimate E_{gap} values with good accuracy [74, 75]. Particularly, it is used in limited cases of infinitely thick samples. The Kubelka–Munk Eq. (1) for any wavelength is described by [74, 75]:

$$F(R_\infty) = \frac{(1-R_\infty)^2}{2R_\infty}\frac{k}{s} \tag{1}$$

where $F(R_\infty)$ is the Kubelka–Munk function or absolute reflectance of the sample, R_∞ is the reflectance, k is the molar absorption coefficient and s is the scattering coefficient. In our case, $BaSO_4$ was adopted as the standard sample in reflectance measurements: $R_\infty = R_{sample}/R_{MgO}$. In a parabolic band structure, the optical band gap and absorption coefficient of semiconductor oxides [76] can be calculated using Eq. (2) [77]:

$$\alpha h\nu = C_1(h\nu - E_{gap})^n \tag{2}$$

where α is the linear absorption coefficient of the material, $h\nu$ is the photon energy, C_1 is a proportionality constant, E_{gap} is the optical band gap and n is a constant associated with

different kinds of electronic transitions ($n = 0.5$ for direct allowed, $n = 2$ for indirect allowed, $n = 1.5$ for direct forbidden, and $n = 3$ for indirect forbidden transitions). From the theoretical calculations, $MgWO_4$ crystals exhibit an optical absorption spectrum governed by direct electronic transitions [78] and E_{gap} for $MgWO_4$ powder was estimated by using $n = 2$ in Eq. (2). The absolute reflectance function described in Eq. (1) with $k = 2\alpha$ with modified Kubelka–Munk equation is given in the Eq. (3):

$$[F(R_\infty)h\nu)^2 = C_2(h\nu - E_{gap}) \quad (3)$$

Hence, $F(R_\infty)$ value can be obtained from Eq. (3) and plotting a graph of $[F(R_\infty)h\nu]^2$ against $h\nu$, E_{gap} values for the $MgWO_4$ powder were calculated by extrapolating the linear portion of the UV–Visible absorption curve.

Figure 6a, b show UV–Vis spectrum of $MgWO_4$ powder synthesized using the CP method and calcined at 900 °C for 2 h, as well as the optimized EBS of $MgWO_4$ crystals calculated by using the DFT method, respectively.

As can be observed in Fig. 6a, the profile of the UV–Vis spectrum for our $MgWO_4$ synthesized using the CP method and calcined at 900 °C for 2 h indicates an optical behavior typical for structurally ordered crystalline materials. The synthesized $MgWO_4$ powder exhibits a direct optical band gap $E_{gap} = 4.33$ eV. According to earlier reports [79–85], $MgWO_4$ ceramics, powders, or crystals present a broad experimental optical band gap ranging from 3.92 to 5.00 eV, which is in good agreement with our obtained results. The electronic band structure provides the electronic transitions in the material from theoretical calculations. From analyzing the EBS, it was noticed that the $MgWO_4$ crystal is characterized by direct electronic transitions between Y↔Y points of the VB and CB in the Brillouin zone as shown in Fig. 6b. This value is in concordance with the experimental UV–Vis spectrum value, but slightly higher ($E_{gap} = 4.49$ eV) because in the theoretical calculations the system has an ideal structure without local defects such as distortions in the octahedral $[MgO_6]/[WO_6]$ clusters.

From the analysis of the DOS, it is feasible to know which orbitals are involved in the VB and the CB in the electronic transition. Figure 7 shows total DOS projected over all atoms involved in the electronic structure of $MgWO_4$ crystals.

The projected DOS on the O atoms is principally determined in the VB by the 2*p* orbitals, while the CB is mainly determined by the 5*d* orbitals from W atoms with minor contributions from the 2*p* and 4*s* orbitals from O and Mg, respectively (Fig. 7). For $MgWO_4$, different M–O bonds in the $[MO_6]$ clusters, where M = Mg and/or W, are expected to have non-degenerate orbitals. In VB, there are contributions of $2p_x$ and $2p_z$ orbitals from O atoms whereas at the bottom of the CB there is a small contribution of the 4 *s* orbitals from Mg atoms and the $5d_z^2$, $5d_{xz}$, and $5d_{x^2-y^2}$ orbitals from W atoms.

It is known that defects play important roles in the properties of a material. Therefore, we created two models with local bonds defects, one with Mg atoms displacement and another with W atoms displacement. The EBS and DOS for these two models are illustrated in the (Supporting Information (SI) section as shown in Figs. SI2(a,b) and SI3(a,b)). Analyzing the results, it is possible to conclude that when the displacement was located on the network modifier (Mg), the defects formed were shallow defects and the creations of new intermediate levels between the VB and CB were not so pronounced with a small decrease of the band gap value to 4.43 eV. However, when the displacement was located on network former (W) the band gap value decreased significantly (2.60 eV) due to the creation of a deep defect in the structure which allowed the creation of new intermediate levels between the VB and CB. Therefore, it is possible to affirm that there are ordered and disordered clusters in the $MgWO_4$ structure.

3.5 Photocatalytic Properties Analyses

Figure 8a–c illustrate the photolysis of RhB, MO, and BCG dyes solutions, while Fig. 8d–f illustrates the PC discoloration of RhB, MO, and BCG dyes by the $MgWO_4$ photocatalyst monitored by the temporal changes in the UV–Vis absorbance spectra of the aqueous dye solutions. The discoloration rates (C_n/C_0) of the RhB, MO, and BCG aqueous dye solutions with and without the $MgWO_4$ catalyst are shown in Fig. 8g–i. The insets show digital photos of RhB, MO, and BCG dyes solutions after different exposure times to UV-light in the presence of the catalyst, and the rate constants (*k*) obtained for the discoloration of RhB, MO, and BCG aqueous dye solutions are illustrated in Fig. 8j–l, respectively.

Figure 8a–c indicates an insignificant reduction of approximately 5%, 6% e 7% of the maximum absorption spectra for the aqueous solutions of RhB, MO, and BCG dyes after 200 min of photolysis, respectively. This behavior indicates a large resistance of the three dyes under UV illumination [79]. As can be observed in Fig. 8d, we did not observe a significant reduction in the concentration of the RhB solution after 200 min of photodiscoloration with the $MgWO_4$ catalyst powder calcined at 900 °C for 2 h using the CP method. Before irradiation, the RhB dye, which is an *N,N,N′,N′*-tetraethylated Rhodamine molecule, had one bandwidth a maximum absorption centered at 543 nm. The photodegradation of RhB dye occurs due to an oxidative attack via active oxygen species on an *N*-ethyl group [79]. The band moved toward *N,N,N′*-tri-ethylated Rhodamine ($\lambda_{max} = 539$ nm), *N,N′*-di-ethylated Rhodamine ($\lambda_{max} = 522$ nm), N-ethylated Rhodamine ($\lambda_{max} = 510$ nm), and Rhodamine ($\lambda_{max} = 498$ nm) species [80]. Therefore,

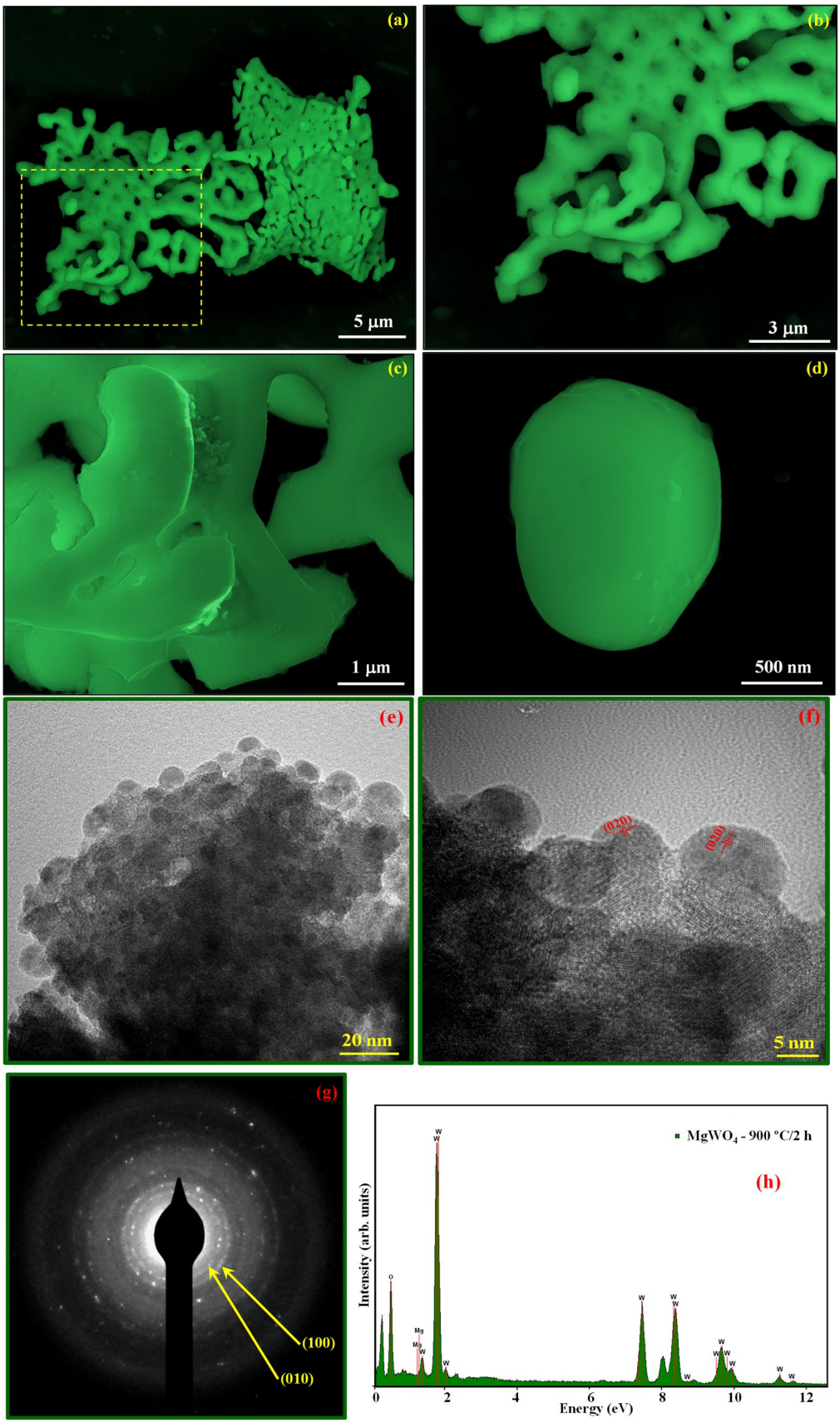
(a)
5 µm
(b)
3 µm
(c)
1 µm
(d)
500 nm
(e)
20 nm
(f)
(020)
(020)
5 nm
(g)
(100)
(010)
MgWO4 - 900 °C/2 h
(h)
Intensity (arb. units)
Energy (eV)
0
2
4
6
8
10
12
O
Mg
W

◂**Fig. 5** FE-SEM images of several $MgWO_4$ powder at **a**, **b** low magnification, **c** medium magnification, and **d** high magnification, respectively. **e** TEM images of several $MgWO_4$ nanopowders at low magnification, **f** HT-TEM images of $MgWO_4$ nanopowders with their respective planes and **g** Indexed SAED patterns of $MgWO_4$ nanopowders, **h** EDS spectrum of several $MgWO_4$ nanopowders, respectively

we assumed that our $MgWO_4$ powder does not have active photocatalytic sites or Lewis basic sites effective for the discoloration of a high percentage of RhB cationic dye after 200 min under UV-light with reduction of approximately 29% (Fig. 8d). According to the literature [86, 87], a high photodegradation rate of cationic dye can be achieved by using visible/irradiation light, activated carbon bimetallic nanocomposite, presence of H_2O_2 and scavengers, such as: dimethyl sulphoxide (DMSO), pbenzoquinone (BQ), tri-ethanolamine (TEOA) and potassium dichromate (PD). Moreover, we confirmed that our $MgWO_4$ nanopowders obtained using the CP method is most efficient photocatalyst for the degradation of the MO anionic dye after 200 min under UV-light (see Fig. 8e). This behavior is probably due to the positively charged surface of our $MgWO_4$ catalyst since the anionic MO dye can be adsorbed more easily than the cationic RhB dye, hence it is easier to be degraded [88] (see Fig. 8d, e). In Fig. 8e, we have noted a discoloration or reduction of approximately 56% at the maximum absorption spectra ($\lambda_{max}=465$ nm) for the aqueous MO dye solutions after 200 min. According to the literature [89], the occurrence of a blue shift ($\lambda_{max}=398$ nm) when employing a photocatalyst with an initial absorbance maximum band comparable with the MO dye ($\lambda_{max}=465$ nm for nonprotonated molecule and $\lambda_{max}=505$ nm for the protonated molecule) indicates that there is still a chromophore group in this intermediate. As can be noted in Fig. 8e, our $MgWO_4$ photocatalyst powder does not promote any maximum band shifts, only a decreasing band with intensity. In general, MO dye solutions with added catalyst, when illuminated under UV-light promote discoloration by forming intermediate species like dimethylaniline, and sodium benzenesulfonate due to the displacement reaction between the dimethyl group of the intermediates and the sodium ion proton, it is transformed into aniline, and benzenesulfonic acid. After being transformed into hydroxy aniline and 4-hydroxybenzenesulfonic acid, it is decomposed into hydroquinone, and *p*-benzoquinone, and is transformed into aliphatic acids such as oxalic acid, which is finally decomposed into CO_2 and H_2O [81, 90–94]. In Fig. 8f we noted a discoloration or reduction of approximately 84% in the maximum absorption spectra ($\lambda_{max}=616$ nm) for the aqueous BCG dye solutions after 200 min. The strong interaction between the alkaline dye and the $MgWO_4$ photocatalyst (Fig. 8e) promotes a significant decrease in the maximum absorbance band of the BCG dye solution [87]. Therefore, $MgWO_4$ powder might be a selective photocatalyst for the discoloration of anionic organics dyes under UV-light [88–90]. We can conclude that our $MgWO_4$ powder has more active photocatalytic sites or Lewis acid sites effective for the discoloration of a high percentage of MO and BCG anionic dyes solutions after 200 min under UV-light (Fig. 8d, e) [91].

To quantitatively understand the reaction kinetics for the discoloration of the three organic dyes: RhB, MO, and BCG by the catalyst powder, as illustrated in Fig. 8g–i, we applied the pseudo-first order model expressed in Eq. (4) to obtain the rate constants (k):

$$-\ln\left(\frac{C_n}{C_0}\right) = kt \tag{4}$$

where, C_0 and C_n is the initial and different concentration of the dye solution of UV-C illumination, t is the time, and k is the pseudo-first order rate constant. This equation is generally used for a photocatalytic discoloration process if the initial concentration of hte pollutant is low (1×10^{-5} mol/L) [92]. According to Eq. (4), a plot of [$\ln(C_n/C_0)$] as a function of t gives a straight line where the slope is k. It is observed from Fig. 8g–i and the corresponding insets, that the $MgWO_4$ photocatalyst powder was more effective and efficient for the discoloration of the MO and BCG dyes, than for the RhB dyes. All the results shown in Fig. 8j–l are absolute and were not normalized for the specific surface area (S_{BET}) of our powder [93]. From Fig. 8j–l, the rate constants in the absence of a catalystor only for the photolysis process of three organic dyes are very small ($k_{(Without\ catalyst/RhB)}=2.626\times10^{-4}$ min^{-1} for RhB, $k_{(Without\ catalyst/MO)}=2.674\times10^{-4}$ min^{-1} for MO, and $k_{(Without\ catalyst/BCG)}=3.495\times10^{-4}$ min^{-1} for BCG), which indicates that there is no significant discoloration of the RhB, MO and BCG dyes after 200 min. Moreover, the rate constants for the discoloration of RhB ($k_{(MgWO_4-Photocatalyst/RhB)}=1.61\times10^{-3}\,min^{-1}$), MO ($k_{(MgWO_4-Photocatalyst/MO)}=3.85\times10^{-3}\,min^{-1}$), and BCG ($k_{(MgWO_4-Photocatalyst/BCG)}=8.862\times10^{-3}\,min^{-1}$) with our $MgWO_4$ powder are shown in Fig. 8g–i. In addition, good coefficient of determination (R^2) and standard deviations (SD) were obtained for all the results, which resulted in high discoloration rates for the MO and BCG dyes. The normalized values for the standard kinetic constant for the $MgWO_4$ powder are shown in Table 3.

The results obtained after the normalization of the kinetic parameters ($k_{(Absolute)}$, $k_{[Normalized]}$ and half lifetime ($\tau_{1/2}$)) of the catalyst powder for photodiscoloration of aqueous RhB, MO, and BCG dye solutions as well as S_{BET} are presented in Table 3, which shows that $k_{[Normalized]}$ values are smaller than $k_{[Absolute]}$ values, i.e., the $MgWO_4$ photocatalyst has a $S_{BET}=0.8$ m^2/g According to the literature [75, 95], $MgWO_4$ ceramics have a low S_{BET} (from 10.46 to 24 m^2/g) and has been scarcely used as a catalyst support. The $k_{[Normalized]}$ values were obtained

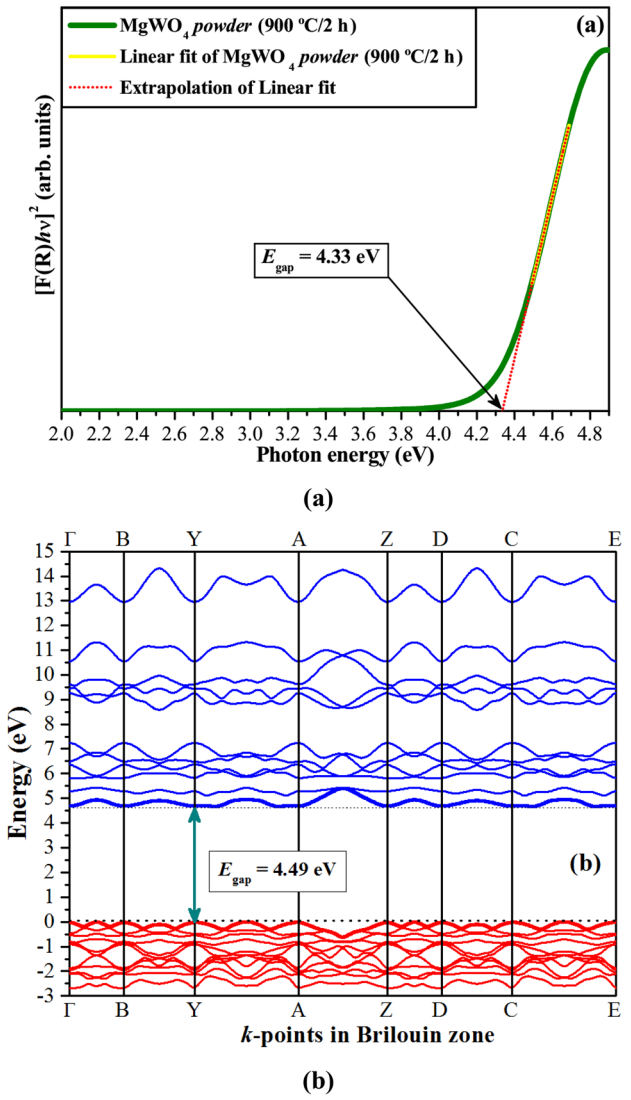

Fig. 6 **a** UV–Vis spectrum of $MgWO_4$ powder and **b** optimized EBS of $MgWO_4$ crystal

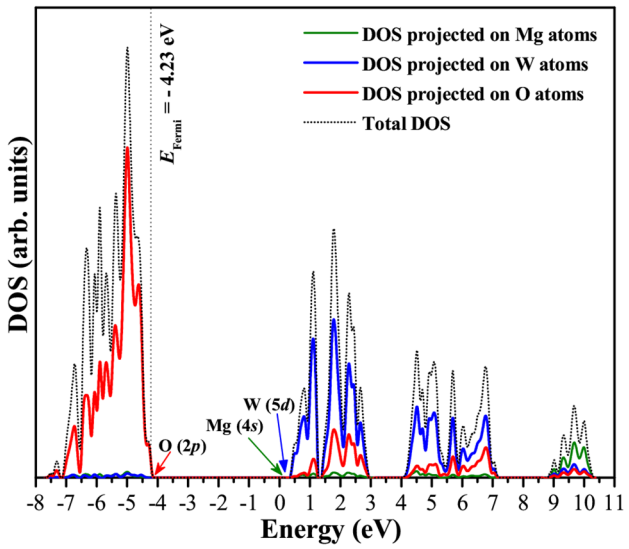

Fig. 7 Projected total DOS on the Mg, W and O orbitals for the $MgWO_4$ crystals

by dividing the $k_{\{absolute\}}$ by the S_{BET} value of $MgWO_4$ photocatalyst, which is presented in Table 3. After normalization, the rate constants of the $MgWO_4$ photocatalyst powder obey the following ascending order: $k_{[MgWO_4-Photocatalyst/BCG]} > k_{[MgWO_4-Photocatalyst/MO]} > k_{[MgWO_4-Photocatalyst/RhB]}$ and after comparing several relationships between the $k_{[MgWO_4-Photocatalyst/BCG]}/k_{[MgWO_4-Photocatalyst/MO]}$, $k_{[MgWO_4-Photocatalyst/BCG]}/k_{[MgWO_4-Photocatalyst/RhB]}$, and $k_{[MgWO_4-Photocatalyst/MO]}/k_{[MgWO_4-Photocatalyst/RhB]}$ values of the $MgWO_4$ photocatalyst powder obtained at 900 °C for 2 h, we observed that the normalized $k_{[MgWO_4-Photocatalyst/BCG]}$ is approximately 2.31 times higher than $k_{[MgWO_4-Photocatalyst/MO]}$, $k_{[MgWO_4-Photocatalyst/BCG]}$ is approximately 5.52 times higher than $k_{[MgWO_4-Photocatalyst/RhB]}$ and $k_{[MgWO_4-Photocatalyst/MO]}$ is approximately 2.39 times higher than $k_{[MgWO_4-Photocatalyst/RhB]}$. The anionic MO and BCG dyes were able to be adsorbed easier than the cationic RhB dye, hence easier to be degraded.

A possible photocatalytic mechanism for the discoloration of RhB, MO and BCG dyes by our photocatalyst $MgWO_4$ powder is represented in Fig. 9a–f, respectively.

In our photocatalytic test, the initial stage is extremely important for the optimization of this process with heterogeneous photocatalysis. This is a very efficient technique for the discoloration of organic pollutants, such as RhB, MO and BCG dyes. In this process, it is necessary to have an optimal dispersion of powder and dyes in the system before irradiation. In the second stage, this well-dispersed system was stirred for 5 min inside a dark box followed by the collection of the first 3 mL aliquot. Subsequently, four UV lights were used to start the photocatalysis [81]. According to the literature [96–101], the presence of order/disorder-types defects or structural distortions in semiconductor oxides facilitates the polarization process, leading to electronic transitions between ordered and disordered clusters, or undistorted and distorted clusters with the formation of e'–$h^{\cdot}$ pairs. In our paper, a wide model based on intermediate electronic levels between VB and CB and complex clusters was proposed to explain the PC activity of $MgWO_4$ powder for the photooxidation of RhB, MO, and BCG dyes. The ideal catalyst powder should have specific features and it should be noted that the most important events occur before excitation, i.e., before irradiation with UV-light ($\lambda = 254$ nm or $h\nu \approx 4.88$ eV) as shown in Fig. 8a. As noted in previous analyses (Rietveld refinement data and theoretical calculations in Support Information with the Figs. S1(a,b) and S2(a,b) to the EBS and DOS displacement in the W and Mg atoms cause changes in the

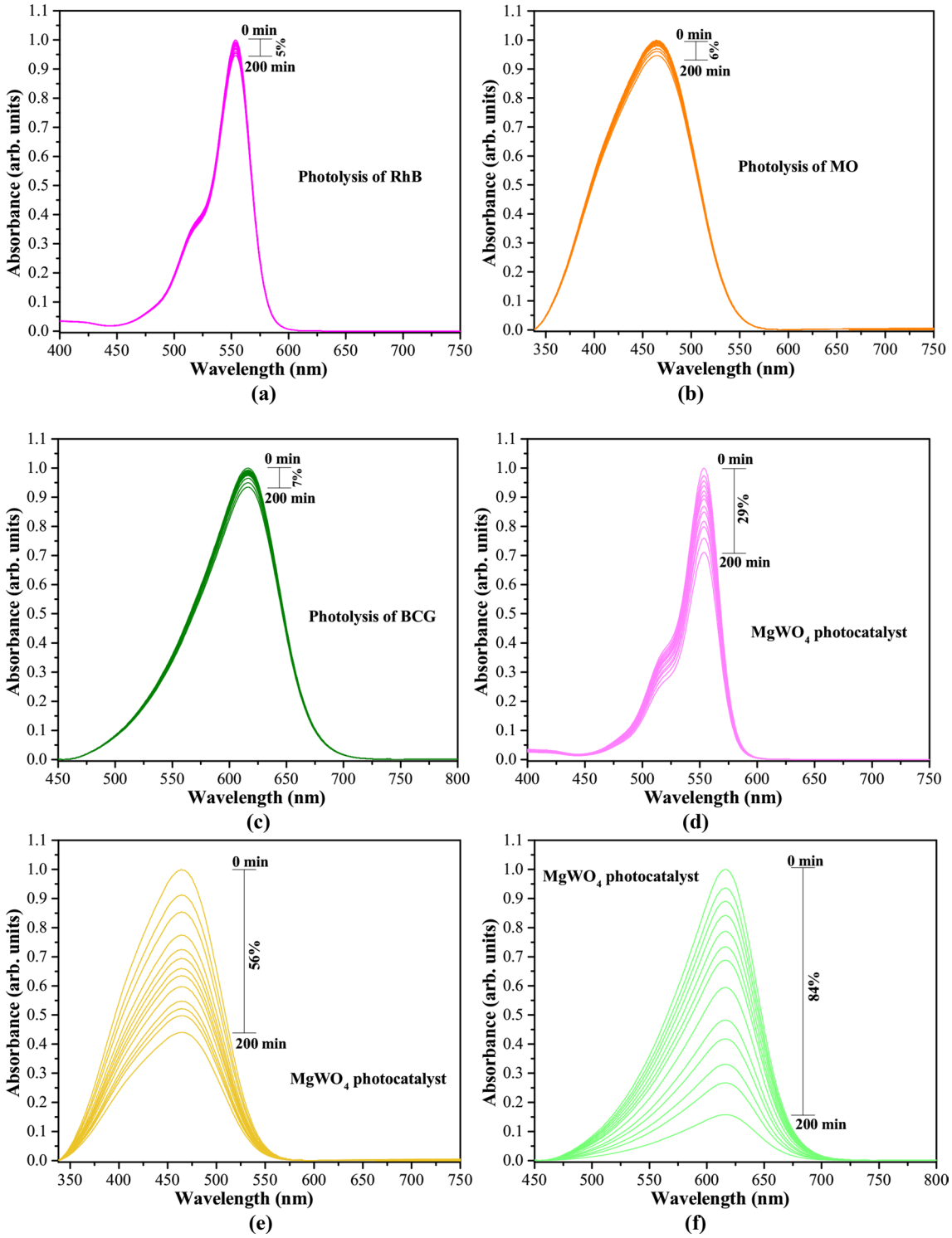

Fig. 8 **a–c** Evolution of UV–Vis absorption spectra after 200 min of illumination without photocatalyst; **d–f** UV–Vis spectra for the photodiscoloration of RhB, MO and BCG dyes using $MgWO_4$ powder; **g–i** kinetics of weight-based photocatalytic discoloration of RhB, MO and BCG dyes by the $MgWO_4$ powder. Insets show digital photodiscoloration photos for RhB, MO and BCG dyes under different UV lamp illumination times; and **j–l** first-order kinetics without and with the catalyst

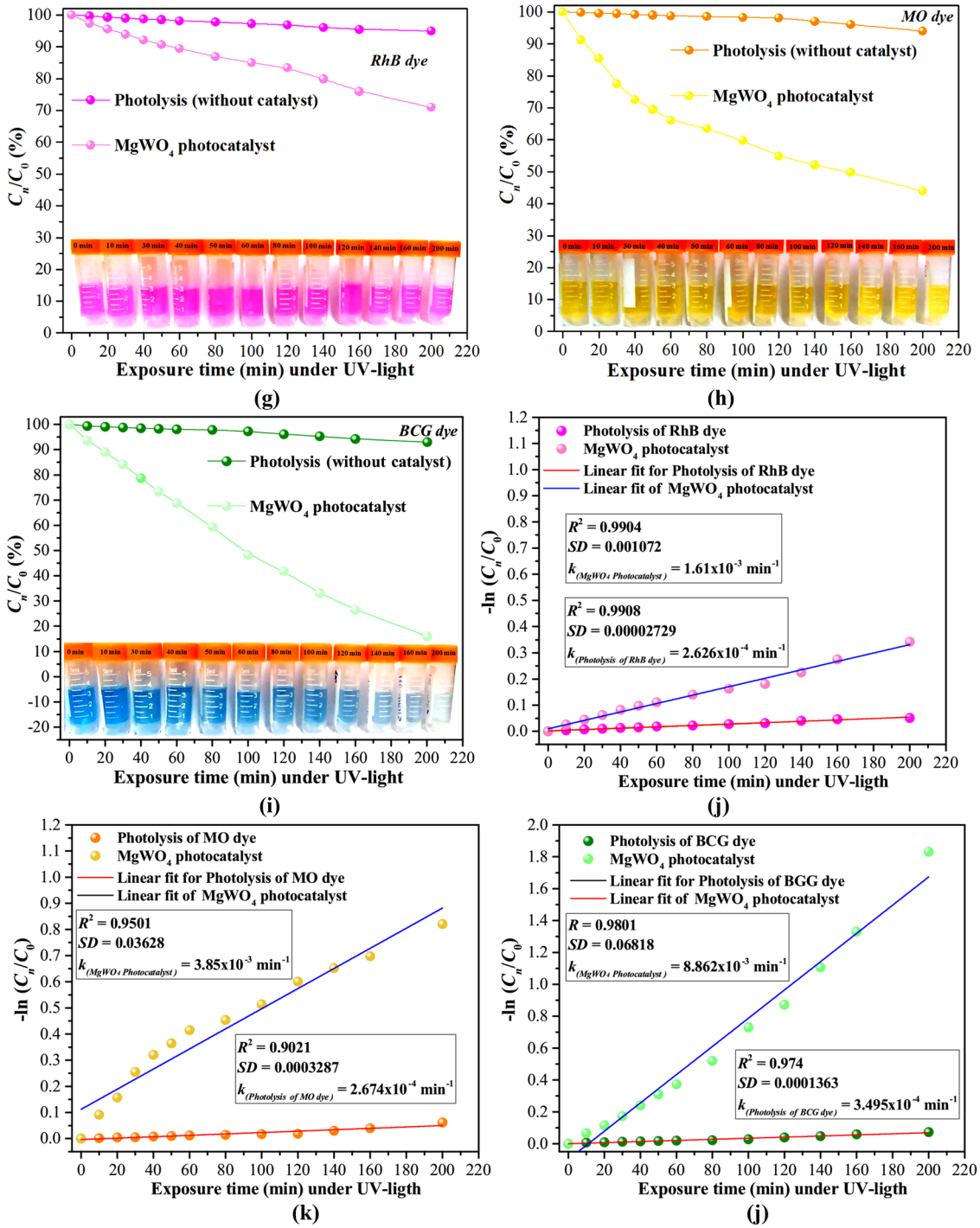

Fig. 8 (continued)

E_{gap} values and different direct transition (Z↔Z) and indirect electronic transition (B↔Y). Therefore, our $MgWO_4$ powder, still has order–disorder structural defects ascribed to different types of distorted clusters $[MgO_6]^x_d - [WO_6]^x_d$ in the VB and ordered $[MgO_6]^x_d - [WO_6]^x_d$ clusters in the CB. In addition, we observed that other characteristics are also very important for improving PC activity in different semiconductor crystals, such as crystallographic preferred orientation, intermediary electronic levels, high surface energy, roughness, defects, high active surface area, facets,

Table 3 Absolute kinetic constants ($k_{(Absolute)}$), normalized kinetic constants ($k_{[Normalized]}$), half-life ($\tau_{1/2}$) and specific surface area (S_{BET}) for different $MgWO_4$ catalyst powder

Samples	$k_{(Absolute)}$ (min^{-1})	S_{BET} (m^2/g)	$k_{[Normalized]}$ (min^{-1}/m^2g)	$\tau_{1/2}$ (min) for $k_{(Abs)}$	$\tau_{1/2}$ (min) for $k_{(Norm)}$	Ref.
wc-RhB	2.626×10^{-4}	–	–	3.064.3	–	◆
wc-MO	2.674×10^{-4}	–	–	2592.2	–	◆
wc-BCG	3.495×10^{-4}	–	–	1983.3	–	◆
*$MgWO_4$-180 °C-12 h/H_2O**	–	10.46	–	–	–	[75]
*$MgWO_4$-180 °C-12 h/H_2O**	–	14.05	–	–	–	[75]
$MgWO_4$-900 °C-2 h/RhB	1.61×10^{-3}	0.8	2.0125×10^{-3}	430.5	344.4	◆
$MgWO_4$-900 °C-2 h/MO	3.85×10^{-3}	0.8	4.8125×10^{-3}	180	144	◆
$MgWO_4$-900 °C-2 h/BCG	8.862×10^{-3}	0.8	1.110775×10^{-2}	78.2	62.4	◆

wc-RhB, wc-MO, and *wc-BCG* = dyes without catalyst, *$MgWO_4$* powder obtained by the CP method heat treated at 900 °C °C for 2 h and used as catalyst to degradation of *RhB, MO* and *BCG* dyes; *H_2O* = Water splitting for $H_{2(g)}$ production; ()* = Absolute and *[]* Normalized by S_{BET} values and $\tau_{1/2}$ is half-life, Ref. = references; ◆ = this work

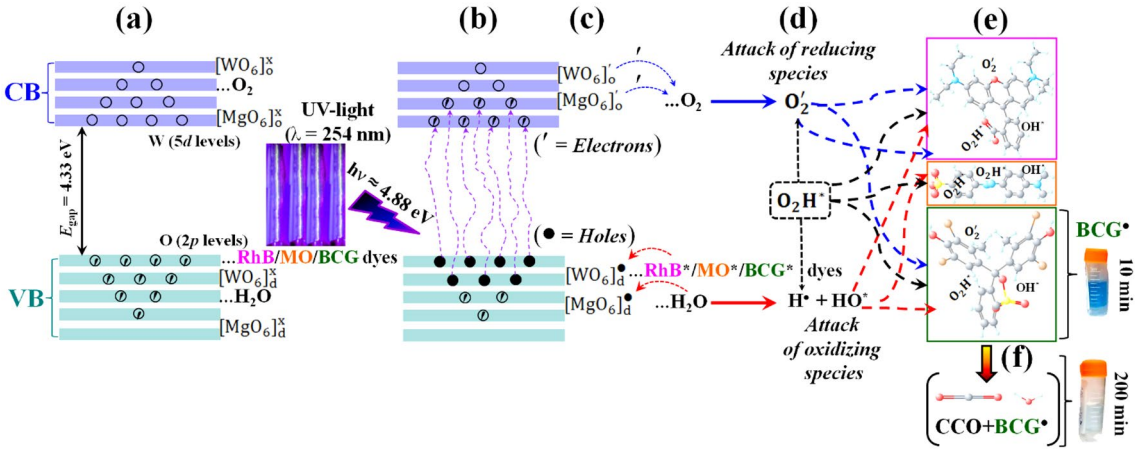

Fig. 9 Proposed photocatalytic reaction mechanism for the discoloration of RhB, MO and BCG dyes solutions using $MgWO_4$ catalyst powder: **a** Broadband model before the start of photocatalysis or photolysis (UV-light off), where the semiconductor is added to the dyes solutions to reach the adsorption–desorption equilibrium between solid–liquid on the electronic transitions between the VB (O 2*p* orbitals) and BC (W 5*d* orbitals), **b** Starting photocatalysis with UV-light. The $MgWO_4$ catalyst powder has order–disorder/distortions in the electronic structure, which promote the formation of intermediate energy levels within the band gap (′ = electrons)/(˙ = holes) pairs and electronic transference between the disordered $[MgO_6]^{\cdot}_{d} - [WO_6]^{\cdot}_{d}$ in the VB and ordered $[MgO_6]'_{o} - [WO_6]'_{o}$ clusters in the CB; **c** Reducing clusters in the VB concede electrons to the CB and oxidizing clusters received electrons from the CB and transference to O_2 and H_2O adsorbed by the $MgWO_4$ catalyst powder by reducing clusters during the discoloration of RhB, MO, and BCG dyes; **d** Defects on the powder surface, which act as catalytic active sites where RhB*, MO*, and BCG* dyes are susceptible to the attack of highly oxidizing species (HO*, O'_2, and O_2H*); **e** Cycles of photooxidation: the discoloration of RhB*, MO*, and BCG* dyes by the formed oxidant radicals occurs; and **f** After several cycles of photodiscoloration H_2O, CO_2 and colorless compounds organic (CCO) form during the mineralization of organic dyes

and adsorption–desorption equilibrium [101, 102]. Figure 9a shows the photocatalytic reaction where the surface of the catalyst can polarize the lattice and lead to possible electronic transitions at the molecular level between disordered $[MgO_6]^{x}_{d}$ and $[WO_6]^{x}_{d}$ clusters and ordered $[MgO_6]^{x}_{d} - [WO_6]^{x}_{d}$ clusters. When UV-light is absorbed by the $MgWO_4$ powder, the following electronics process of charge transfer between between species involved can occur, as expressed in Eqs. (5–8) below:

$$\xrightarrow{\text{In the dark}} MgWO_{4(defects)} \rightarrow [MgO_6]_d^x - [WO_6]_o^x \quad (5)$$

$$\xrightarrow{\text{In the dark}} MgWO_{4(defects)} \rightarrow [WO_6]_d^x - [MgO_6]_o^x \quad (6)$$

$$\xrightarrow{h\nu=4.88\ eV} MgWO_{4(defects)} \rightarrow [MgO_6]_d^x - [WO_6]_o^x \xrightarrow{\text{Electron transfer}} [MgO6]_d^{\cdot} - [WO_6]_o' \quad (7)$$

$$\xrightarrow{h\nu=4.88\ eV} MgWO_{4(defects)} \rightarrow [WO_6]_d^x - [MgO_6]_o^x \xrightarrow{\text{Electron transfer}} [WO_6]_d^{\cdot} - [MgO_6]_o' \quad (8)$$

As shown in Fig. 9b, we propose that the disordered/distorted octahedral $[MgO_6]_d^{\cdot}$ and $[WO_6]_d^{\cdot}$ clusters are located inintermediate levels near the VB, whereas the ordered octahedral $[MgO_6]_o'$ and $[WO_6]_o'$ clusters are located in intermediate levels below the CB. This process leads to the formation of $' \leftrightarrow {}^{\cdot}$ pairs within the powder band gap and also on the semiconductor surface as shown in Fig. 9c. During the photooxidation processes, the reducing $[MgO_6]_d^{\cdot} - [WO_6]_d^{\cdot}$ clusters located in the VB react with the adsorbed H_2O and/or RhB, MO, and BCG dyes, while the undistorted or ordered $[MgO_6]_o' - [WO_6]_o'$ clusters located in the CB interact with the adsorbed oxygen (O_2) species,as shown in Eqs. (9–14):

$$[WO_6]_o' - [MgO_6]_d^{\cdot} + H_2O \rightarrow [WO_6]_o' - [MgO_6]_d^{\cdot}H_2O_{(ads)} \quad (9)$$

$$[MgO_6]_o' - [WO_6]_d^{\cdot} + H_2O \rightarrow [MgO_6]_o' - [WO_6]_d^{\cdot}H_2O_{(ads)} \quad (10)$$

$$[WO_6]_o' - [MgO_6]_d^{\cdot} + H_2O_{(ads)} \rightarrow [WO_6]_o' - [MgO_6]_d^x + OH_{(ads)}^* + H^{\cdot} \quad (11)$$

$$[MgO_6]_o' - [WO_6]_d^{\cdot} + H_2O_{(ads)} \rightarrow [MgO_6]_o' - [WO_6]_d^x + OH_{(ads)}^* + H^{\cdot} \quad (12)$$

$$[WO_6]_o' - [MgO_6]_d^x + HO_{(ads)}^* \rightarrow [WO_6]_o' - [MgO_6]_d^xHO^* \quad (13)$$

$$[MgO_6]_o' - [WO_6]_d^x + OH_{(ads)}^* \rightarrow [MgO_6]_o' - [WO_6]_d^xOH^* \quad (14)$$

In the CB, the oxidizing $[MgO_6]_o'$ and $[WO_6]_o'$ clusters located on the semiconductor surface are able to react with the $O_{2(ads)}$ molecules by means of electron transference process. Before this process, the $H^{\cdot}$ species in Eqs. (11) and (12) are able to interact with the superoxide radical anion (O_2') resulting in the formation of perhydroxyl radical (O_2H^*) as given in Fig. 9d and presented in Eqs. (15–18):

$$[MgO_6]_d^{\cdot} - [WO_6]_o' + O_{2(ads)} \rightarrow [MgO_6]_d^{\cdot} - [WO_6]_o^x + O_{2(ads)}' \quad (15)$$

$$[WO_6]_d^{\cdot} - [MgO_6]_o' + O_{2(ads)} \rightarrow [WO_6]_d^{\cdot} - [MgO_6]_o^x + O_{2(ads)}' \quad (16)$$

$$[MgO_6]_d^{\cdot} - [WO_6]_o^x + O_{2(ads)}' + H^{\cdot} \rightarrow [MgO_6]_d^{\cdot} - [WO_6]_o' + O_2H^* \quad (17)$$

$$[WO_6]_d^{\cdot} - [MgO_6]_o^x + O_{2(ads)}' + H^{\cdot} \rightarrow [WO_6]_d^{\cdot} - [MgO_6]_o' + O_2H^* \quad (18)$$

Moreover, RhB, MO and BCG dyes are also excited by UV-light, as shown in Fig. 9d and presented in Eqs. (19–21):

$$\xrightarrow{h\nu=4.88\ eV} \text{RhB dye} \rightarrow \text{RhB}^* \text{ dye} \quad (19)$$

$$\xrightarrow{h\nu=4.88\ eV} \text{MO dye} \rightarrow \text{MO}^* \text{ dye} \quad (20)$$

$$\xrightarrow{h\nu=4.88\ eV} \text{BCG dye} \rightarrow \text{BCG}^* \text{ dye} \quad (21)$$

These cycles occur continuously while the system is exposed to UV-light. Finally, after several photooxidation cycles (200 min), the discoloration of RhB*, MO* and BCG* dyes by OH*, O_2' and O_2H^* radicals occurs, as shown in Fig. 9e, f and indicated by Eqs. (22–24) [102]:

$$\xrightarrow{h\nu=4.88\ eV} \text{RhB} * \text{dye} \xrightarrow{OH*,\ O_2',\ \text{and}\ O_2H^*} CCO + CO_2 + H_2O \quad (22)$$

$$\xrightarrow{h\nu=4.88\ eV} \text{MO} * \text{dye} \xrightarrow{OH*,\ O_2',\ \text{and}\ O_2H^*} CCO + CO_2 + H_2O \quad (23)$$

$$\xrightarrow{h\nu=4.88\ eV} \text{BCG} * \text{dye} \xrightarrow{OH*,\ O_2',\ \text{and}\ O_2H^*} CCO + CO_2 + H_2O \quad (24)$$

where, CCO = colorless compounds organic.

Figure 9a–f displays the photocatalytic mechanism in which the defects on the crystal surface and the electronic structure of the distorted/disordered $[MgO_6]_d^{\cdot}$ and $[WO_6]_d^{\cdot}$ clusters and ordered $[MgO_6]_o'$ and $[WO_6]_o'$ clusters play an important role in the production of O H^*, O_2', and O_2H^* radicals, which are the most oxidizing species in these chemical reactions for the discoloration or mineralization of the organic RhB, MO and BCG dyes in aqueous solution.

4 Conclusions

In summary, we successfully obtained $MgWO_4$ powder by using the CP method after calcination at 900 °C for 2 h. The XRD/SAED patterns and Rietveld refinement data indicate that the $MgWO_4$ powder presents a wolframite-type monoclinic structure, space group (P_2/c) and symmetry point group (C_{2h}^4). Our electron density maps showed an inhomogeneous distribution of charges between distorted octahedral [MgO_6] clusters. FE-SEM, TEM and HR-TEM images showed that the powders are composed by several particles with irregular morphologies, non-uniform particles size and agglomerated nature. EDS spectra revealed the chemical composition of $MgWO_4$ powders. The existence of different E_{gap} values between the experimental $MgWO_4$ powder and theoretical $MgWO_4$ crystal is attributed to the existence of localized electronic levels within the forbidden band gap. We concluded that these energy states derive particularly from distortions on both octahedral [MgO_6] and [WO_6] clusters at the short and medium range. The theoretical calculations indicated that the EBS of $MgWO_4$ crystals is characterized by direct electronic transitions. According to the DOS analyses, the energy states in the VB consist of the 2*p* orbitals from O, while in the CB the 5*d* orbitals from W contribute to the energy states. Furthermore, we investigated the PC discoloration properties for three organic dyes: RhB, MO, and BCG. The results of the PC activity indicated that our $MgWO_4$ powder has more active photocatalytic sites or Lewis acid sites effective for the discoloration of a high percentage of MO and BCG anionic dyes after 200 min under UV-light. Moreover, we proposed a photocatalytic mechanism based on a wide model related to the presence of intermediate electronic levels between the VB and CB and complex clusters proved by theoretical calculations. Finally, we proposed to explain that the optical band gap values near the UV illumination energy (4.88 eV), defects on the crystal surface, and the electronic structure are the probable pathway for homogeneous MO and BCG dyes photodiscoloration in the presence of H_2O and O_2 dissolved is homolysis of excited MO* and BCG* dyes into radicals. The OH^*, $O_2^{'}$ and O_2H^* radicals formed are the most oxidizing species in these chemical reactions for the discoloration of the organic RhB, MO, and BCG dyes in aqueous solution to CCO, CO_2 and H_2O.

Acknowledgment The authors acknowledge the financial support of the Brazilian research financing institutions: CNPq (304531/2013-8, 150949/2018-9, 312318/2017-0 and 479644/2012-8), FAPESP (2012/14004-5, 2013/26671-9 and 2017/11986-5), and CAPES.

References

1. G. Sharma, M. Naushad, D. Pathania, A. Kumar, Desalin. Water Treat. **57**, 19443–19455 (2016)
2. G. Sharma, A. Kumar, K. Devi, S. Sharma, M. Nausha, A.A. Ghfar, T. Ahama, F.J. Stadler, Int. J. Biol. Macromol. **114**, 295–305 (2018)
3. G. Sharma, A. Kumar, M. Nausha, A. García-Peñas, A.H. Al-Muhtaseb, A.A. Ghfar, V. Sharma, T. Ahamad, F.J. Stadler, Carbohyd. Polym. **202**, 444–453 (2018)
4. G. Sharma, S. Bhogal, M. Naushad, A. Kumar, F.J. Stadler, J. Photochem. Photobiol. **347**, 235–246 (2017)
5. G. Sharma, B. Thakur, M. Naushad, A.H. Al-Muhtaseb, A. Kumar, M. Sillanpaa, G.T. Mola, Mater. Chem. Phys. **193**, 129–139 (2017)
6. G. Sharma, D. Pathania, M. Naushad, N.C. Kothiyal, Chem. Eng. J. **215**, 413–421 (2014)
7. G. Sharma, S. Bhogal, V.K. Gupta, S. Agarwal, A. Kumar, D. Pathania, G.T. Mola, F.J. Stadler, J. Mol. Liq. **275**, 499–509 (2019)
8. G. Sharmaa, A. Kumar, S. Sharma, A.H. Al-Muhtaseb, M. Naushad, A.A. Ghfar, T. Ahamad, F.J. Stadler, Sep. Purif. Technol. **211**, 895–908 (2019)
9. T. Montini, V. Gombac, A. Hammed, L. Felisari, G. Adami, P. Fornasiero, Chem. Phys. Lett. **498**, 113–119 (2010)
10. H. Zhang, R.J. Bai, C. Lu, J. Li, Y.G. Xu, L.B. Kong, M.C. Liu, Ionics **25**, 533–540 (2019)
11. J. Ruiz-Fuertes, S. López-Moreno, D. Errandonea, J. Pellicer-Porres, R. Lacomba-Perales, A. Segura, P. Rodríguez-Hernández, A. Muñoz, A.H. Romero, J. González, J. Appl. Phys. **107**, 083506–1–083506-10 (2010)
12. M.A.P. Almeida, L.S. Cavalcante, M. Siu Li, J.A. Varela, E. Longo, J. Inor. Organomet. Polym. Mater. **22**, 264–270 (2012)
13. Q. Gou, O.J. Kleppa, Thermochim. Acta **288**, 53–61 (1996)
14. E.K. Kazenas, Y.V. Tsvetkov, I.O. Samoilova, G.K. Astakhova, A.A. Petrov, V.A. Volchenkova, Russ. Metall. (Metally) **2004**, 320–324 (2004)
15. M. del Arco, D. Carriazo, S. Gutiérrez, C. Martín, V. Rives, Inorg. Chem. **43**, 375–384 (2004)
16. L. Jin-Qing, Y. Chuang-Tao, M. Jian-Xin, Chin. J. Lumin. **30**, 327–331 (2009)
17. Y. Zu, Y. Zhang, K. Xu, F. Zhao, RSC Adv. **6**, 31046–31052 (2016)
18. J.R. Günter, M. Amberg, Solid State Ion. **32**(33), 141–146 (1989)
19. M. Amberg, J.R. Günter, H. Schmalle, G. Blasse, J. Solid State Chem. **77**, 162–169 (1988)
20. L.L.Y. Chang, M.G. Scroger, B. Phillips, J. Am. Ceram. Soc. **49**, 385–390 (1966)
21. R.C. Pullar, S. Farrah, N.M. Alford, J. Eur. Ceram. Soc. **27**, 1059–1063 (2007)
22. V.B. Mikhailik, L. Vasylechko, H. Kraus, V. Kapustyanyk, M. Panasyuk, Y. Prots, V. Tsybulskyy, J. Phys. Stud. **14**, 3201-1–3201-11 (2010)
23. M. Gancheva, A. Naydenov, R. Iordanova, D. Nihtianova, P. Stefanov, J. Mater. Sci. **50**, 3447–3456 (2015)
24. L. Zhang, Y. Huang, S. Sun, F. Yuan, Z. Lin, G. Wang, J. Lumin. **169**, 161–164 (2016)
25. C.S. Lim, Asian J. Chem. **24**, 1519–1522 (2012)
26. X. Feng, W. Feng, M. Xia, K. Wang, H. Liu, D. Deng, X. Qin, W. Yao, W. Zhu, RSC Adv. **6**, 14826–14831 (2016)
27. J. Li, C. Yang, J. Meng, J. Chin. Rare Earth Soc. **27**, 730–734 (2009)
28. N.R. Krutyak, D.A. Spassky, I.A. Tupitsyna, A.M. Dubovik, Opt. Spectr. **121**, 45–51 (2016)

29. L. Li, Y. Yu, G. Wang, L. Zhang, Z. Lin, CrystEngComm **15**, 6083–6089 (2013)
30. J. Huang, B. Tian, J. Wang, Y. Wang, W. Lu, Q. Li, L. Jin, C. Li, Z. Wang, CrystEngComm **20**, 608–614 (2018)
31. P.D. Bhuyan, D. Singh, S. Kansara, P. Yadav, S.K. Gupta, Y. Sonvane, S.K. Rout, E. Sinha, J. Mater. Sci. **52**, 4934–4943 (2017)
32. N. Krutyak, V.V. Mikhailin, D. Spassky, I.A. Tupitsyna, A.M. Dubovik, Inter. Conf. Oxide Mater. Electr. Eng. OMEE. **2012**, 235–236 (2012)
33. V.B. Mikhailik, H. Kraus, V. Kapustyanyk, M. Panasyuk, Y. Prots, V. Tsybulskyi, L. Vasylechko, J. Phys. Cond. Matter. **20**, 365219–1–365219-8 (2008)
34. M. Guo, G. Dou, S. Gong, D. Zhou, J. Eur. Ceram. Soc. **32**, 883–890 (2012)
35. M. Guo, G. Dou, G. Li, S. Gong, J. Mater. Sci. Mater. Electr. **26**, 608–612 (2015)
36. R. Ullah, R.N. Malik, A. Qadir, Afr. J. Environ. Sci. Technol. **3**, 429–446 (2009)
37. D.M.A. Costa, A.C.B. Júnior, Holos. **21**, 81–101 (2005)
38. F.C.C. Assis, S. Albeniz, A. Gil, S.A. Korili, R. Trujillano, M.A. Vicente, L. Marçal, M. Saltarelli, K.J. Ciuffi, Desalin. Water Treat. **39**, 316–322 (2012)
39. L.F. Fernandes, A.C. Wosiak, L. Domingues, C.V. Pacheco, P.E. Lagos, Curitiba: Sanepar v. 1: 1–500 (2005)
40. Z. Carmen, S. Daniela, *Organic pollutants ten years after the stockholm convention—environmental and analytical update* (InTech, Croatia, 2012), pp. 55–86. **Chapter 3**
41. Y. Na, S. Song, Y. Park, Korean J. Chem. Eng. **22**, 196–200 (2005)
42. M. Soylak, Y.E. Unsal, E. Yilmaz, M. Tuzen, Food Chem. Toxicol. **49**, 1796–1799 (2011)
43. R. Jain, M. Mathur, S. Sikarwar, A. Mittal, J. Environ. Manage. **85**, 956–964 (2007)
44. R.G. Sandberg, G.H. Henderson, R.D. White, E.M. Eyring, J. Phys. Chem. **76**, 4023–4025 (1972)
45. R.A.G. de Oliveira, T.B. Zanoni, G.G. Bessegato, D.P. Oliveira, G.A. Umbuzeiro, Quim. Nova. **37**, 1037–1046 (2014)
46. A.A.L.R. Al-Rubaie, R.J. Mhessn, E-J. Chem. **9**, 465–470 (2012)
47. L.F. Silva, O.F. Lopes, V.R. Mendonça, K.T.G. Carvalho, E. Longo, Photochem. Photobiol. **92**, 371–378 (2016)
48. W. Xin, D. Zhu, G. Liu, Y. Hua, W. Zhou, Int. J. Photoenergy. **2012**, 767905–1–767905-7 (2012)
49. F.R. Zaggout, J. Disper. Sci. Technol. **26**, 757–761 (2005)
50. S. Delanghe, W. Van Biesen, N. Van de Velde, S. Eloot, A. Pletinck, E. Schepers, G. Glorieux, J.R. Delanghe, M.M. Speeckaert, Clin. Chem. Lab. Med. **56**, 436–440 (2018)
51. I. Kazeminezhad, A. Sadollahkhani, J. Mater. Sci.: Mater. Electr. **27**, 4206–4215 (2016)
52. K. Kabra, R. Chaudhary, R.L. Sawhney, Ind. Eng. Chem. Res. **43**, 7683–7696 (2004)
53. L.S. Cavalcante, J.C. Sczancoski, V.C. Albarici, J.M.E. Matos, J.A. Varela, Mater. Sci. Eng. B. **150**, 18–25 (2008)
54. J.W. England, J. Pharmacol. Sci. **1**, 440–443 (1912)
55. T. Salmi, E. Paatero, P. Nyholm, Chem. Eng. Process. Process Intensif. **43**, 1487–1493 (2004)
56. M. Kakihana, M. Yoshimura, Bull. Chem. Soc. Jpn. **72**, 1427–1443 (1999)
57. H.M. Rietveld, J. Appl. Crystallogr. **2**, 65–71 (1969)
58. M. Bortolotti, L. Lutterotti, I. Lonardelli, J. Appl. Cryst. **42**, 538–539 (2009)
59. L. Lutterotti, M. Bortolotti, G. Ischia, I. Lonardelli, H.R. Wenk, Z. Kristallogr, Krist. **26**, 125–130 (2007)
60. M. Bortolotti, I. Lonardelli, J. Appl. Cryst. **46**, 259–261 (2013)
61. S. Brunauer, P.H. Emmett, E. Teller, J. Am. Chem. Soc. **60**, 309–319 (1938)
62. R. Dovesi, V.R. Saunders, C. Roetti, R. Orlando, C.M. Zicovich-Wilson, F. Pascale, B. Civalleri, K. Doll, N.M. Harrison, I.J. Bush, P. D'Arco, M. Llunel, M. Causà, Y. Noël, *CRYSTAL14 User's Manual*, Italy (2014)
63. A.D. Becke, J. Chem. Phys. **96**, 2155–2160 (1992)
64. A.F. Gouveia, J.C. Sczancoski, M.M. Ferrer, A.S. Lima, M.R.M.C. Santos, M. Siu lI, R.S. Santos, E. Longo, L.S. Cavalcante, Inorg. Chem. **53**, 5589–5599 (2014)
65. http://www.crystal.unito.it/basis-sets.php
66. F. Corà, A. Patel, N.M. Harrison, R. Dovesi, C.R.A. Catlow, J. Am. Chem. Soc. **118**, 12174–12182 (1996)
67. R.C. de Oliveira, L. Gracia, M. Assis, M. Siu Li, J. Andres, L.S. Cavalcante, E. Longo, CrystEngComm **18**, 6483–6491 (2016)
68. E.L.S. Souza, J.C. Sczancoski, I.C. Nogueira, M.A.P. Almeida, M.O. Orlandi, M.S. Li, R.A.S. Luz, M.G.R. Filho, E. Longo, L.S. Cavalcante, Ultrason. Sonochem. **38**, 256–270 (2017)
69. O.S. Filipenko, E.A. Pobedimskaya, V.I. Ponomarev, N.V. Belov, Kristallogr. **13**, 1073–1075 (1968)
70. H.M. Rietveld, Acta Crystallogr. **22**, 151–152 (1967)
71. K. Momma, F. Izumi, J. Appl. Crystallogr. **41**, 653–658 (2008)
72. K. Momma, F. Izumi, J. Appl. Crystallogr. **44**, 1272–1276 (2011)
73. L.S. Cavalcante, E. Moraes, M.A.P. Almeida, C.J. Dalmaschio, N.C. Batista, J.A. Varela, E. Longo, M. Siu Li, J. Andrés, A. Beltrán, Polyhedron **54**, 13–25 (2013)
74. R.A. Smith, *Semiconductors*, 2nd edn. (Cambridge University Press, London, 1978), pp. 1–535
75. J. Meng, T. Chen, X. Wei, J. Wei, J. Li, Z. Zhang, RSC Adv. **9**, 2567–2571 (2019)
76. R. Lacomba-Perales, J. Ruiz-Fuertes, D. Errandonea, D. Martínez-García, A. Segura, Europhys. Lett. **83**, 37002–37006 (2008)
77. S. Dey, R.A. Ricciardo, H.L. Cuthbert, P.M. Woodward, Inorg. Chem. **53**, 4394–4399 (2014)
78. S. Wannapop, T. Thongtem, S. Thongtem, Appl. Surf. Sci. **258**, 4971–4976 (2012)
79. I.A. Kamenskikh, V.N. Kolobanov, V.V. Mikhailin, I.N. Shpinkov, D.A. Spassky, Nucl. Instr. Meth. Phys. Res A. **467–468**, 1423–1425 (2001)
80. E.A.A. Júnior, F.X. Nobre, G.S. Sousa, L.S. Cavalcante, M.R.M.C. Santos, F.L. Souza, J.M.E. de Matos, RSC Adv. **7**, 24263–24281 (2017)
81. Y. Zhao, C. Li, X. Liu, F. Gu, J. Alloys Compd. **440**, 281–286 (2007)
82. T. Wu, G. Liu, J. Zhao, H. Hidaka, N. Serpone, J. Phys. Chem. B. **102**, 5845–5851 (1998)
83. I. Fajriati, M. Mudasir, E.T. Wahyuni, Int. J. Adv. Chem. Eng. Biol. Sci. **1**, 21–24 (2014)
84. T. Chen, Y. Zheng, J.-M. Lin, G. Chen, J. Am. Soc. Mass Spectr. **19**, 997–1003 (2008)
85. H. Lee, Y.K. Park, S.J. Kim, B.H. Kim, H.S. Yoon, S.-C. Jung, J. Ind. Eng. Chem. **35**, 205–210 (2016)
86. G. Sharma, A. Kumar, S. Sharma, M. Naushad, T. Ahamad, A.H. Al-Muhtaseb, M. Naushad, F.J. Stadler, S.I. Al-Saeedi, G.M. Al-Senani, N.S. Al-kadhi, F.J. Stadler, J. Mol. Liq. **272**, 170–179 (2018)
87. G. Sharma, D.D. Dionysiou, S. Sharma, A. Kumar, A.H. Al-Muhtaseb, M. Naushad, F.J. Stadler, Catal. Today. **335**, 437–451 (2019)
88. W. Zhong, T. Jiang, Y. Dang, J. He, S.Y. Chen, Appl. Catal. A. Gen. **549**, 302–309 (2018)

89. M.U.D. Sheikh, G.A. Naikoo, M. Thomas, M. Bano, F. Khan, New J. Chem. **40**, 5483–5494 (2016)
90. S. Xie, P. Huang, J.J. Kruzic, X. Zeng, H. Qian, Sci. Rep. **6**, 21947–21956 (2016)
91. S. Yang, C. Ye, X. Song, L. He, F. Liao, RSC Adv. **4**, 54810–54818 (2014)
92. B. Saha, S. Das, J. Saikia, G. Das, J. Phys. Chem. C. **115**, 8024–8033 (2011)
93. L. Parimala, J. Santhanalakshmi, React. Kinet. Mech. Catal. **109**, 393–403 (2013)
94. J. Xiao, H. Zhang, Y. Xia, Z. Li, W. Huang, RSC Adv. **6**, 39861–39869 (2016)
95. V.N. Kolosov, V.M. Orlov, M.N. Miroshnichenko, T.Yu. Prokhorova. IOP Conf Ser Mater Sci Eng **704**, 012011 (2019)
96. C. Martín, P. Malet, V. Rives, G. Solana, J. Catal. **169**, 516–526 (1997)
97. R.A. Roca, J.C. Sczancoski, I.C. Nogueira, M.T. Fabbro, H.C. Alves, L. Gracia, L.P.S. Santos, C.P. de Sousa, J. Andrés, G.E. Luz Jr., E. Longo, L.S. Cavalcante, Catal. Sci. Technol. **5**, 4091–4107 (2015)
98. L.S. Cavalcante, F.M.C. Batista, M.A.P. Almeida, A.C. Rabelo, I.C. Nogueira, N.C. Batista, J.A. Varela, M.R.M.C. Santos, E. Longo, M. Siu Li, RSC Adv. **2**, 6438–6454 (2012)
99. L.S. Cavalcante, J.C. Sczancoski, N.C. Batista, E. Longo, J.A. Varela, M.O. Orlandi, Adv. Powder Technol. **24**, 344–353 (2013)
100. G. Botelho, J. Andres, L. Gracia, L.S. Matos, E. Longo, ChemPlusChem. **81**, 202–212 (2016)
101. G. Byzynski, C. Melo, D.P. Volanti, M.M. Ferrer, A.F. Gouveia, C. Ribeiro, J. Andrés, E. Longo, Mater. Des. **120**, 363–375 (2017)
102. W.S. Pereira, J.C. Sczancoski, Y.N.C. Calderon, V.R. Mastelaro, G. Botelho, T.R. Machado, E.R. Leite, E. Longo, Appl. Surf. Sci. **440C**, 61–72 (2018)